

## Symmetrical collision of multiple vortex rings

R. H. Hernández, and T. Reyes

Citation: [Physics of Fluids](#) **29**, 103604 (2017); doi: 10.1063/1.5004587

View online: <https://doi.org/10.1063/1.5004587>

View Table of Contents: <http://aip.scitation.org/toc/phf/29/10>

Published by the [American Institute of Physics](#)

---

### Articles you may be interested in

[A method to control and analyze vortex ring collisions in the laminar regime](#)

Scilight **2017**, 160006 (2017); 10.1063/1.5006639

[Antisymmetric vortex interactions in the wake behind a step cylinder](#)

Physics of Fluids **29**, 101704 (2017); 10.1063/1.4991530

[Low-Reynolds-number flow around a wall-mounted square cylinder: Flow structures and onset of vortex shedding](#)

Physics of Fluids **29**, 103601 (2017); 10.1063/1.4989745

[Collisions of droplets on spherical particles](#)

Physics of Fluids **29**, 103305 (2017); 10.1063/1.5005124

[Reducing spin-up time for simulations of turbulent channel flow](#)

Physics of Fluids **29**, 105101 (2017); 10.1063/1.4993489

[Kolmogorov's Lagrangian similarity law revisited](#)

Physics of Fluids **29**, 105106 (2017); 10.1063/1.4993834

---

PHYSICS TODAY

WHITEPAPERS

ADVANCES IN PRECISION  
MOTION CONTROL

Piezo Flexure Mechanisms  
and Air Bearings

READ NOW

PRESENTED BY

**PI**

# Symmetrical collision of multiple vortex rings

R. H. Hernández<sup>a)</sup> and T. Reyes

LEAF-NL, Departamento de Ingeniería Mecánica, Universidad de Chile, Casilla 2777, Santiago, Chile

(Received 31 January 2017; accepted 12 September 2017; published online 11 October 2017)

In this work, we investigate the motion, interaction, and simultaneous collision between many initially stable vortex rings arranged symmetrically in two initial configurations, three and six rings making an angle of 60 and 120° between their straight path lines, respectively. We report results for laminar vortex rings in air obtained through numerical simulations of the ring velocity, pressure, and vorticity fields, both in free flight and during the entire collision. Each collision was studied for small Reynolds numbers  $Re < 10^3$  based on both the self-induced velocity and diameter of the ring. The case of three rings produces secondary vortical structures formed by laterally expanding dipolar arms with top and bottom secondary vortex rings. The case of six colliding rings produces, as secondary structures, two big rings moving in opposite directions, a process that reminds us of the head-on collision of two rings [T. T. Lim and T. B. Nickels, “Instability and reconnection in the head-on collision of two vortex rings,” *Nature* **357**, 225–227 (1992)] under a hypothetical time reversal transformation. Both collisions display a characteristic kinetic energy evolution where mean collision stages can be identified within the range of Reynolds numbers investigated here. *Published by AIP Publishing.* <https://doi.org/10.1063/1.5004587>

## I. INTRODUCTION

The symmetrical instability of azimuthal waviness observed during the head-on collision between two vortex rings may lead to the reconnection of vortex filaments followed by the formation of radially moving (diverging) smaller rings.<sup>1</sup> The wavelength and the instability spatial azimuthal phase are responsible of the number of reconnection points and thus the number of newly formed rings. The reconnection mechanism is responsible for the creation of subsequent secondary structures that may again interact developing an energy cascade supported on further smaller structures.<sup>2</sup> Such colliding ring situations represent a particular scenario where the energy flows from two big vortices, which redistribute vorticity, into a cascade of smaller spatial scales. If the energy is dissipated in connection with the systematic production of smaller scales by virtue of vortex reconnection, then ring collisions may be considered as a mechanism to create turbulence.<sup>3</sup>

But it seems not always true that vortex reconnections go into smaller secondary structures.<sup>4</sup> Sometimes the interaction between two rings of a given size may lead to secondary structures of higher size and therefore smaller wavenumber.<sup>5</sup> The size of these structures relies on the way the vortex lines of opposite strength come close together convecting vorticity away from the initial contact region.<sup>6</sup> In the case of symmetrical ring collisions, the role of the initial configuration determines not only the family but also the size of the secondary vortex structures<sup>7,8</sup> and thus the way the system energy is dissipated. Secondary structures produced by such symmetrical collisions<sup>4</sup> may however display a very complex time evolution, undergoing periodic oscillations that,

in some cases, may favour unexpected reconnections and thus leading to a very different energy distribution.<sup>7</sup> The primary goal of this paper is to address the questions arising from the collision of multiple vortex rings by fully resolving the Navier-Stokes equations in three dimensions. In order to mimic as close as possible a real experiment, we create rings from vortex generators located at the faces of the numerical domain. Vortex rings are launched into the center of the domain where the collision takes place. This paper is organized as follows: Section II defines and describes the physical problem, the numerical method, and simulation details. Section III shows results for single rings, and subsequent results for the ring collision in air are presented in Sec. III A for 3 rings and Sec. III B for 6 rings. The energy of the collision is discussed in Sec. III D. Concluding remarks are summarised in Sec. IV.

## II. PROBLEM FORMULATION

A vortex ring is a compact and tridimensional fluid structure where vorticity  $\omega(\mathbf{r}, t)$  is distributed into an axisymmetric torus-like region called the vortex ring core. The fluid circulation or strength  $\Gamma(t)$  in a closed path around the vortex core is related to the vortex ring diameter,  $D$ , the amount of vorticity, and the type of vorticity distribution in the vortex core of size  $a$ . The cooperative effect of fluid circulation around different portions of the ring makes the rings self-propelled structures having a very definite direction of motion. The self-induced ring velocity  $U_a$  and the amount of momentum associated with a ring will depend on the ring properties and, indirectly, on the way the ring has been created.<sup>9</sup> Self-propelled laminar rings may travel important distances before slowing down by the effect of both viscous losses and the shedding of vorticity.

<sup>a)</sup>Author to whom correspondence should be addressed: roherman@ing.uchile.cl. URL: <http://www.leafnl.uchile.cl>.

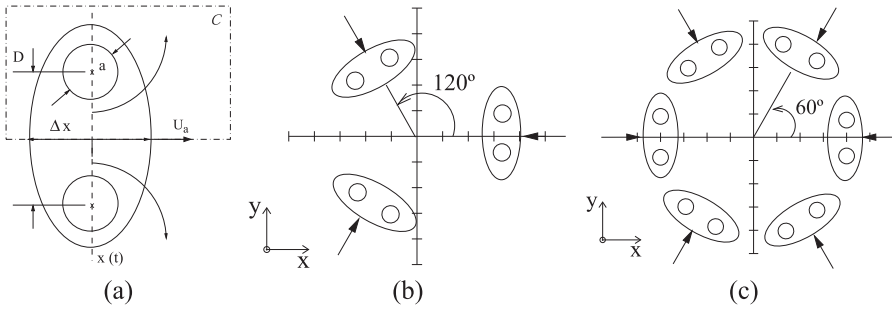


FIG. 1. Collision configuration. (a) A vortex ring of diameter  $D$ , vortex core size  $a$ , and self-induced velocity  $U_a$  are the basic ingredients of the collision. (b) Three identical rings, initially forming an angle of  $120^\circ$  between their direction of motion, are launched simultaneously toward an aiming point. (c) Under a similar configuration, six identical rings, forming an angle of  $60^\circ$ , are launched to the central point.

In Fig. 1(a), we show the schematic dimensions of a ring. In order to evaluate the ring's circulation  $\Gamma$  with Eq. (1), a contour path around the ring core is considered. In Fig. 1(a), a sketch of the contour path  $C$  is shown. The circulation  $\Gamma$  is written as

$$\Gamma = \oint_C \mathbf{v} \cdot d\mathbf{l}. \quad (1)$$

For a given velocity field  $\mathbf{v} = (u(\mathbf{r}, t), v(\mathbf{r}, t))$ , with coordinates  $\mathbf{r} = (x, y)$ , the circulation  $\Gamma(t)$  is computed over the path  $C$  using the local velocity in the frame moving with the vortex ring, i.e., if the self-induced velocity is in the  $x$  direction, then  $u(\mathbf{r}, t) \rightarrow u(\mathbf{r}, t) - U_a$ , where  $U_a$  should be previously estimated.<sup>10,11</sup>

Our problem can be summarized in 3 stages: We start simulating (i) the generation procedure of vortex rings, (ii) followed by their propagation within the domain, and (iii) the collision between 3 or 6 rings within the computational domain.

In this work, we will adopt a different vortex generation method than in previous numerical simulation studies;<sup>2</sup> we obtain the velocity and pressure conditions at the nozzle from the simulation of an upstream chamber where a flat piston motion is modeled. The ring's generating mechanism attempts to mimic, as close as possible, the generation conditions of recent experiments,<sup>12</sup> ensuring both initial collision

symmetries and angles of the starting rings.<sup>7</sup> In order to generate 3 and 6 vortex rings [see Figs. 1(b) and 1(c)], we define a nozzle of diameter  $D_0$  located on the face of a hexagonal calculation domain. On the external faces of the vortex generator, a piston velocity signal  $U_p(t)$  represents the displacement of a piston-type mechanism, driving the fluid inside the chamber. This mechanism will therefore produce a discharge of fluid through the nozzles at the inner faces of each vortex generator.

The hexagonal geometry automatically defines the direction of motion of the rings aiming towards the center of the domain, producing symmetric collisions (see Fig. 2). The dimensions of the generation chamber are defined in such a way that the edge conditions do not affect the development of the vortex ring; thus, the faces of the ring generator are  $L_w \sim 10D_0$  and the transverse size of the hexagonal domain is  $2L_w \sim 20D_0$ .<sup>5</sup> To ensure the natural development of the vorticity structures in the  $z$  axis, i.e., perpendicular to the collision plane, the height of the chamber is  $L_z = 20D_0$  which provides enough room for further evolution of the collision.

## A. Governing equations

For an incompressible Newtonian fluid in the absence of gravity, the equations that govern the problem are the mass

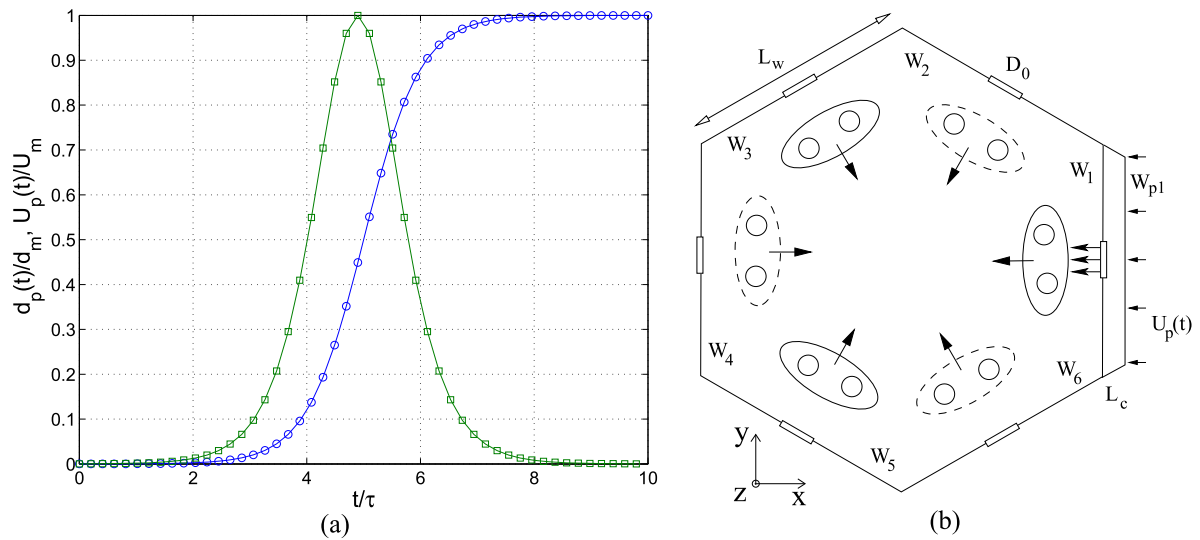


FIG. 2. (a) S-shaped forcing signal  $d_p(t)$  ( $\square$ ) representing the normalized piston position in time in the chamber. The resulting piston velocity  $U_p(t) = \dot{d}_p(t)$  ( $\circ$ ) is imposed over each domain rear face  $W_{pj}$  corresponding to face  $W_j$ . Its maximum value is  $U_m$  and the average velocity at the nozzle exit is  $U_0$ . (b) Schematic boundary conditions imposed on rear facing walls  $W_{pj}$  (with  $j = 1-6$ ) in the generation of vortex rings created in nozzles of faces  $W_1$ ,  $W_4$ , and  $W_5$  for the 3R case and on the faces  $W_1$  to  $W_6$  for the 6R case. Each wall of length  $L_w$  and height  $L_z$  has its own nozzle-like hole of diameter  $D_0 = 15$  (mm) where  $L_w/D_0 \sim 10$  y  $L_z/D_0 = 20$ . The buffer cavity formed between each pair of walls  $W_j$  and  $W_{pj}$  has width  $L_c/D_0 = 1$  and it is closed at the top and bottom.

conservation equation (2) and the Navier Stokes equation for momentum (3),

$$\nabla \cdot \mathbf{v} = 0, \quad (2)$$

$$\frac{\partial \mathbf{v}}{\partial t} + \mathbf{v} \cdot \nabla \mathbf{v} = -\frac{1}{\rho} \nabla p + \mu \nabla^2 \mathbf{v}, \quad (3)$$

where  $\rho$  and  $\nu$  are the density and kinematic viscosity of the fluid, respectively. The velocity field  $\mathbf{v}(\mathbf{r}, t)$  as well as the pressure field  $p(\mathbf{r}, t)$  are computed on the entire domain, including the volume at the upstream chamber where the forcing signal  $U_p(t)$  is imposed.

## B. Computation domain and boundary conditions

In order to generate the vortex rings simultaneously, the driving signal  $U_p(t)$  shown in Fig. 2(a) is imposed simultaneously on each external rear facing wall of the hexagonal domain ( $W_{pj}$  with  $j = 1 \rightarrow 6$ ) as shown in Fig. 2(b). The velocity signal corresponds to the time derivative of the piston stroke  $d_p(t)$  function located on each side of the domain. The resulting piston pulse-like velocity creates a ring at each nozzle that will naturally move toward the center of the domain.

It is important to remark here that this condition allows the formation of a wall boundary layer profile inside the nozzle which evolves into a jet-like profile at the nozzle exit.<sup>13</sup>

The way we produce a velocity profile at the nozzle exit differs completely from others' where it is imposed using pre-determined velocity programs.<sup>14,15</sup> The nozzle exit profile in such studies is a combination of smoothed top hat functions, in time and space, using hyperbolic functions. In our case, a hyperbolic tangent function drives the piston position inside the buffer chamber (cf. Fig. 2). The rings obtained with these methods are similar to our rings; however, we have the advantage to determine the mechanics of the velocity profile at the nozzle exit and determine some elements on the velocity profile, like the inflexion point during the transition from the boundary layer to jet-like flow at the nozzle exit.<sup>13</sup> Nevertheless, even if our method is far more expensive in computational resources, the control of the signal timing allows us to investigate during the ring formation process the transition associated with the formation number.<sup>9</sup> Our piston velocity program looks for a smooth motion of the piston avoiding sharp transitions which can be accomplished with a hyperbolic tangent function, smooth enough to avoid discontinuities produced by, for instance, a linear ramp motion of the piston. The forcing function that gives life to the velocity program was first implemented years ago in experimental studies<sup>11,12</sup> where a piston based vortex generator was driven by a loudspeaker, a 2<sup>nd</sup> order system with a flat response in the low frequency limit below typical resonances. The idea here is to derive a velocity driven motion as close as possible with our experimental tests.

The piston stroke  $d_p(t)$  corresponds to a smooth hyperbolic function represented in Eq. (4), where the velocity of the piston is calculated as  $U_p(t) = \dot{d}_p(t)$ ,

$$d_p(t) = \frac{d_0}{2} \left( 1 + \tanh \left( \frac{t - t_0}{\tau} \right) \right). \quad (4)$$

The parameter  $t_0$  represents a given time delay for the piston motion, while  $\tau$  is the characteristic rise time of the signal

and the maximum piston stroke is represented by  $d_0$ . The smooth initial ramp of the hyperbolic function drives here the piston position rather than imposing the piston velocity.<sup>14</sup> This type of signal has been also used in recent numerical studies to generate vorticity rings interacting with passive scalar distributions.<sup>16</sup> The rings created can be characterised by the Reynolds number defined as  $Re = U_a D_0 / \nu$ , a notation far more easy to compute than the strength ( $\Gamma$ ) based Reynolds number.

In order to mimic the piston effect, the signal  $U_p(t)$  works as a time varying boundary condition applied on the rear facing walls  $W_{p1}, W_{p3}$ , and  $W_{p5}$  of Fig. 2(b) for the case of three rings and on the faces  $W_{p1}$  to  $W_{p6}$  in the case of six rings. Under such a configuration, we create a buffer cavity (width  $L_c$ ) between  $W_1$  and  $W_{p1}$  walls, running along the entire vertical coordinate and closed at the top and bottom. Once the  $U_p(t)$  impulsive signal is on, the flow field is computed inside the buffer cavity resulting in vorticity sheets rolling outward the nozzle and thus creating a ring. The remaining faces are considered smooth rigid walls where the fluid velocity vanishes. However, as we do not know *a priori* the final size of the vortex structures produced by the collision, the upper and lower surfaces of the domain are open to the atmosphere and are kept at atmospheric pressure condition  $P_a$ .

For example, the boundary conditions for the case of 3 rings are summarised here,

$$\left\{ \begin{array}{ll} W_{p1}, W_{p3}, W_{p5} & \longrightarrow u = (u_x^2 + u_y^2)^{-1/2} = U_p(t), u_z = 0 \\ W_{p2}, W_{p4}, W_{p6} & \longrightarrow u_x = u_y = u_z = 0 \\ W_{j=1 \rightarrow 6} & \longrightarrow u_x = u_y = u_z = 0 \\ z = -10D_0, z = 10D_0 & \longrightarrow \mathbf{r} = (x, y, z), p(\mathbf{r}) = P_a \end{array} \right\}. \quad (5)$$

The reader may find the domain geometry and the way the nozzles work in the numerical simulation unusual. It is far more simple, easy, and less expensive in computing time to do what most numerical simulations on vortex rings dynamics usually do: start either with the Dirichlet boundary condition at the nozzle section imposing an uniform velocity profile<sup>17</sup> or with an initial velocity field computed from the Biot-Savart analogy for vortex filaments with a given vorticity distribution at the vortex ring core.<sup>2,4</sup> Here however we decided to keep the vortex generation model as close as possible with experimental methods, in order to have vorticity sheets freely forming at the nozzle edges which engages a realistic ring development.

## C. Numerical method

The governing equations are solved in the laminar regime using the software Fluent.<sup>18</sup> The solver used in the calculations is pressure based and a semi-implicit formulation of the equations is adopted.

We solve the transient equations considering a fluid at constant temperature and normal conditions. The solver is based on the SIMPLEC algorithm<sup>19</sup> to correct the velocity field over each iteration. The convergence criteria applied here are such that the maximum residual falls below  $10^{-4}$  for both the momentum and continuity equations.

In the 1st order temporal discretisation, the time step used is  $\Delta t = 10^{-3}$  s, and the number of iterations per time step is variable because it is determined by the convergence criteria. The choice of this small time step ensures a good temporal resolution in order to detect even the velocity gradients at the nozzle output during the ring formation stage. Each numerical simulation extends for 2 physical seconds requiring almost 2 days of calculation in a 24-processor Dell cluster. A detailed description of the governing equations and other aspects of the simulation can be found in the documentation of the code.<sup>18</sup>

In order to balance the relationship between the precision of the results and the computational load, a grid independence test was carried out. Three discrete grids of the entire domain were built up [grids are fine (1), mid (2), and coarse (3)]. We have varied the grid structure during the volume meshing as well as the number of tetrahedral type elements.

From a base geometry and type of discretisation, a linear growth factor  $\alpha$  is implemented in order to determine the grid element size allowing to mesh the whole volume but increasing the spatial resolution in regions where velocity gradients are important, for instance, in the ring's path.

The grid performance is evaluated estimating the error in the discretisation as it is recommended in Ref. 20. This procedure consists in defining a representative cell or grid size called  $h$  [Eq. (6)] on a line, area, or volume, depending on the variable to be analysed. In our case, a volume analysis (subscript *vol*) and a linear analysis (subscript *linear*) were performed.

The objective of this volume meshing analysis is to evaluate the accuracy of the results at a global level between the 3 different grids. The linear analysis is performed in order to evaluate the accuracy along the transverse axis of the ring, where we determine the ring's velocity profile as well as other ring properties. The values of  $h$  are calculated from Eq. (6) and they are summarised in Table I, where the total domain volume,  $h_{vol}$ , considered for the calculation is of the order of  $2.25 \times 10^{-2}$ , and the linear section lengths along  $z$  are used in the computation of  $h_{linear}$ , 0.101 m,

$$h = \left[ \frac{1}{N} \sum_{k=1}^N (\Delta l_k) \right]^{(1/n)}, \quad (6)$$

where  $\Delta l_k$  is the length or volume along the  $k$ -cell,  $N$  is the number of cells along this section, and  $n$  is the dimension where the analysis is being performed.

In Ref. 20, a grid refinement factor must satisfy the recommended condition  $r = h_{coarse}/h_{fine} > 1.3$ . In Table I, we show the resulting factors we have obtained for the volumetric and linear mesh analyses.

According to the grid size analysis, we conclude that in order to balance the computational load and to ensure reasonable precision in the results, the midsize grid will be used. It presents a lower error in the estimation of the variables and the associated computational load is approximately 40% lower than in the case of the fine grid.

### III. RESULTS

Once the impulsive velocity signal  $U_p(t)$  completes its cycle, the vortex rings have run through several nozzle diameters  $D_0$  in their path into the center of the domain. The self-induced velocity  $U_a$  of a ring is proportional to the circulation  $\Gamma$  which will depend on the piston velocity and therefore average nozzle velocity.<sup>9</sup>

It follows that a suitable velocity scale during the ring launching is  $U_0$  defined by the mean at the nozzle exit for each Reynolds number during the piston stroke [cf. Eq. (4)],

$$U_0 = (1/\tau) \int_0^\tau u_n(t) dt, \quad (7)$$

where  $u_n(t)$  represent time series of nozzle velocity.

At each time step, the rings can be visualised by plotting a single iso-vorticity surface which, in our cases, correspond to a value  $|\omega(\mathbf{r}, t)| = 30\%$  of the maximum vorticity found for  $t > t_0$ . This practice allows us to track a torus-like shaped ring where the vorticity is mostly concentrated into the vortex bubble.

The ring's travel in free flight will depend on the geometry of collision. For instance, in the collision of 6 rings, they may travel nearly  $8D_0$  before colliding with the other neighbour rings, but in the case of 3 rings, the travel increases almost half a diameter before they may reach the neighbour rings. Some typical recording of the main properties of the rings in free flight before collision is displayed in Fig. 3.

Once a ring is launched from the nozzle, its behaviour is determined by the loss of circulation  $\Gamma$  as we observe in Fig. 3(a). The effect of  $\Gamma$  on both the self-induced velocity and ring diameter is shown in Figs. 3(b) and 3(c) where the monotonic increase in the ring diameter is accompanied with a decrease of the self-induced velocity as well. This behaviour can be interpreted with the aid of the Saffman formula given by

$$U_a = \frac{\Gamma}{4\pi R} \left( \ln \frac{8R}{a} - \beta \right), \quad (8)$$

where parameter  $\beta$  depends on the type of vorticity distribution with  $\beta = 0.558$  for a Gaussian vorticity core distribution displaying a time varying core growth  $a = \sqrt{4\nu t}$  valid for thin vortex rings ( $R \gg a$ ).<sup>21-23</sup>

TABLE I. Mesh types with progressive linear grid refinement (linear factor  $\alpha$ ) of element of initial size  $\Delta_i$  and final size  $\Delta_f$ .

Grid	$\Delta_i$ (m)	$\alpha$	$\Delta_f$ (m)	$N_{vol}$	$h_{vol}$ (m)	$r_{vol}$	$N_{linear}$	$h_{linear}$ (m)	$r_{linear}$
(1)	$0.2 \times 10^{-3}$	1.1	$10 \times 10^{-3}$	$6.56 \times 10^5$	$3.24 \times 10^{-3}$	...	387	$0.25 \times 10^{-3}$	...
(2)	$0.3 \times 10^{-3}$	1.1	$10 \times 10^{-3}$	$2.89 \times 10^5$	$4.27 \times 10^{-3}$	$r_{21} = 1.31$	280	$0.35 \times 10^{-3}$	$r_{21} = 1.41$
(3)	$0.4 \times 10^{-3}$	1.2	$10 \times 10^{-3}$	$1.08 \times 10^5$	$5.92 \times 10^{-3}$	$r_{32} = 1.38$	213	$0.46 \times 10^{-3}$	$r_{32} = 1.31$

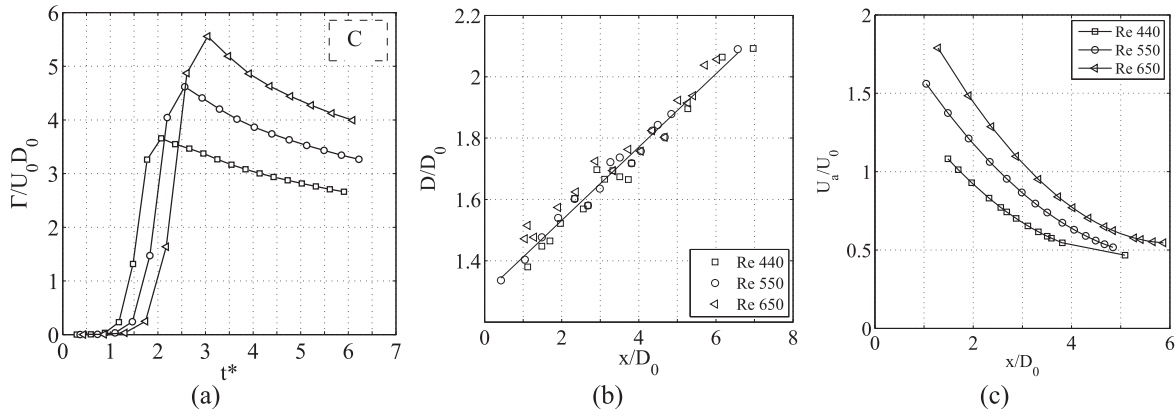


FIG. 3. (a) Single ring run. (a) Evolution of the ring circulation  $\Gamma$  computed on the contour  $C$  of Fig. 1, as a function of dimensionless time  $t^* = tU_a/D_0$ . (b) The diameter growth as a function of the distance from the nozzle exit. (c) The self-induced velocity of the ring.  $Re = 440$  ( $\square$ ),  $Re = 550$  ( $\circ$ ), and  $Re = 650$  ( $\triangle$ ).

When we operate simultaneously the 3 (or 6) vortex generators using the same forcing signal, we can launch 3 (or 6) identical vortex rings which travel in free flight almost  $\sim 8D_0$  before colliding with their neighbours. In Secs. III A and III B, we present the mechanism and resulting secondary structures in the collision of 3 and 6 vortex rings.

### A. Collision of 3 rings (3R)

Figure 4 shows the temporal progression of the collision between three identical rings. Once the formation process is completed, they move in a straight path line toward the collision zone ( $0.05 < t < 0.45$  s). The characteristic diameter increases while the self-induced velocity, circulation, and kinetic energy decrease slightly as we will show later.

For  $0.65 < t < 1.15$  s, the rings are very close and the lateral vorticity tubes of side-by-side rings make contact, and as adjacent vortex tubes have opposite sign vorticity, they lead to a local dipolar coupling generating local dipolar structures (like vortex dipoles) that move in the opposite direction to

the original rings. This mechanism explains the further radial expansion of the final vortex structure.<sup>1</sup>

During this stage, the reconnection of the lateral tubes is followed by the reconnection of the upper vorticity tubes of the rings, giving rise to two new rings that are ejected in a direction perpendicular to the direction of the collision. The overall collision is in good agreement with the experimental results of Ref. 5.

In Fig. 4, for  $t > 1.15$  the reconnection is complete and we have secondary structures driving the last stage of what we call post-collision flow. We observe that the three arm-like dipolar structures drive radially but the two top and bottom secondary rings perform a natural stretching of the flow in the  $z$  coordinate.

In Fig. 5, we display typical velocity profiles of one of the rings (3R case) at three different distances  $1D_0$ ,  $2D_0$ , and  $3D_0$  from the nozzle exit. We plot the absolute value of local velocity, in agreement with similar experimental results from hot-wire anemometry.<sup>12</sup> The amplitude of the forcing signal

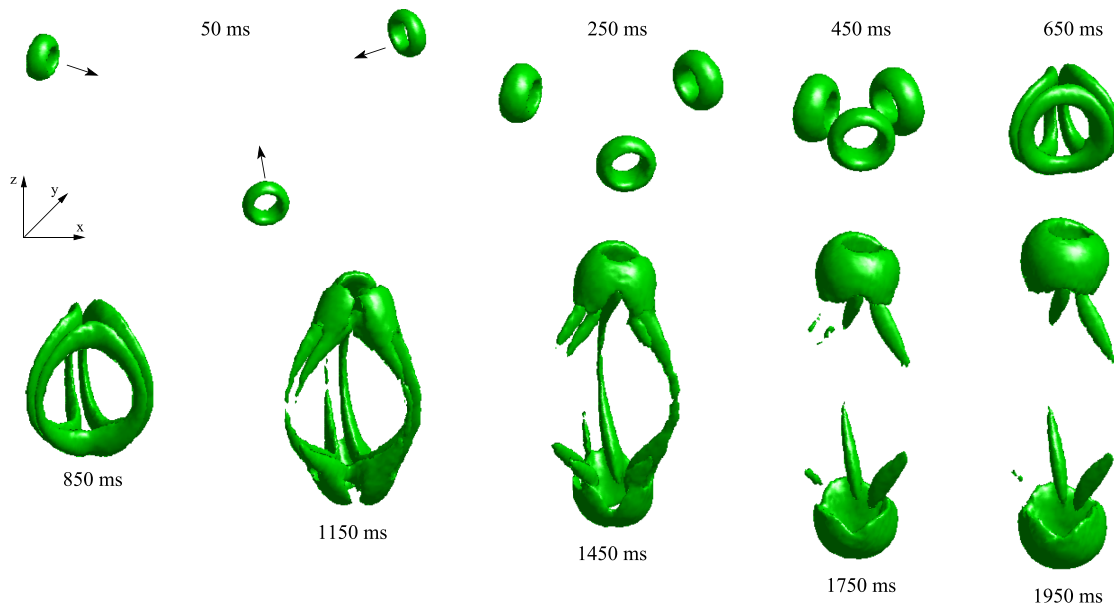


FIG. 4. 3R collision. Time evolution of the vorticity iso-surface  $|\omega(\mathbf{r}, t)| = 30\%$  of the maximum vorticity value at each successive time after  $t_0$  in Eq. (4) for  $Re = 440$ .

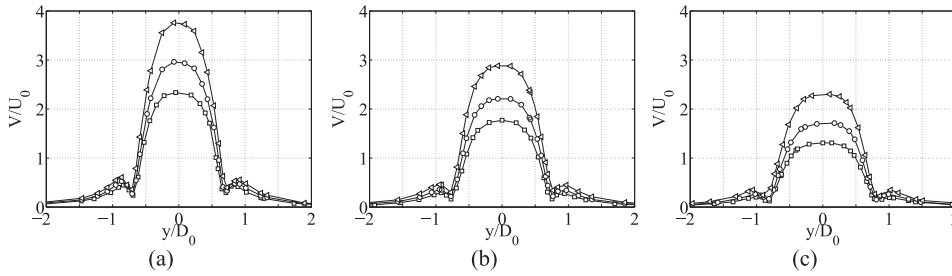


FIG. 5. 3R collision. Absolute velocity profiles of the rings ( $V = |v|$ ) at different distances from the nozzle exit and different Reynolds numbers (a)  $1D_0$ , (b)  $2D_0$ , (c)  $3D_0$  at  $Re = 440$  ( $\square$ ),  $Re = 550$  ( $\circ$ ), and  $Re = 650$  ( $\triangleleft$ ).

determines the value of the Reynolds number and therefore determines the self-induced velocity of a ring.<sup>23</sup> For each position  $x/D_0$ , we have plotted the velocity profiles at three Reynolds numbers. These profiles are normalised with  $U_0$  the average velocity at the nozzle exit. As it may be expected, the higher the Reynolds number  $Re$ , the faster the ring moves. After normalisation, we observe a systematic increase of the central velocity with the Reynolds number at each location  $x/D_0$  but little influence on the ring diameter as the profiles collapse on the abscissa. The same analysis performed for one of the rings of the 6 ring configuration revealed a very similar result (not shown). This should be expected since the rings are identical and at  $x = 3D_0$  in any of the two situations; they do not yet experience a mutual influence since the contact between rings begins approximately at  $x \sim 7.8D_0$  for 6 rings and at  $x \sim 8.4D_0$  for 3 rings, i.e., almost half a diameter farther from the nozzle.

Figure 6 shows the vorticity profile of a ring in absolute values,  $|\omega|$ , for  $x = D_0, 2D_0, 3D_0$  from the nozzle exit. The amplitude of the vorticity decreases rapidly as the ring moves away from the nozzle. For each plot, it seems that the Reynolds number determines the initial amplitude of ring's core vorticity which is in fact an effect of piston velocity. These profiles do not differ from the 6R case as the mutual influence between rings in the pre-collision stages begins when the lateral vortex tubes of each ring come into contact. In the normalisation

of the vorticity profile, we used  $\omega_0 \sim U_0/(D_0/2)$  as a characteristic shear scale at the nozzle exit and we get a better collapse of the different profiles than in the case of the velocity profiles.

### 1. 3R secondary structures

In Fig. 7, we display different views of the secondary structures formed during the collision of three rings. Once the vortex rings have travelled a distance of about  $x = 8.4D_0$  from the nozzle exit, we observe the first contact between the lateral vortex tubes which is the starting point in the formation of secondary structures of the collision.

Figure 8(a) shows the absolute velocity profiles across the transverse axis of a lateral arm-like dipolar structure at a distance  $1D_0$  from the collision center of the domain. It can be seen that as the Reynolds number increases, the velocity increases however the characteristic dimensions of the dipoles are found to be insensitive with the Reynolds number. The position of the lateral maxima and minima is approximately the same for all three curves.

The velocity components  $v_x$  and  $v_y$  are shown in Figs. 8(b) and 8(c). It is observed a predominance of the velocity component  $v_x$  which determines the direction of motion of the dipole resulting in the radial progression of the dipolar arms shown in Fig. 7.

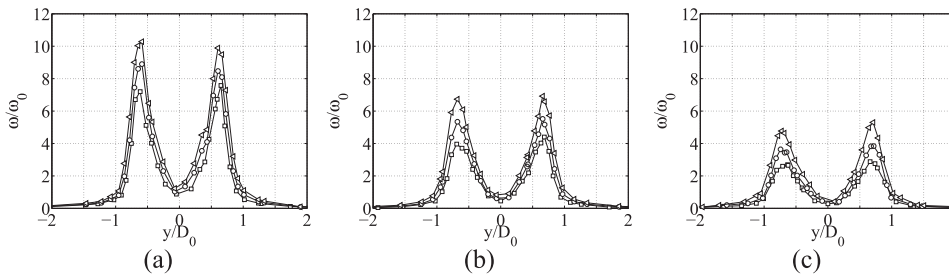


FIG. 6. 3R collision. Absolute vorticity profiles of the rings ( $\omega = |\omega|$ ) at different distances from the nozzle exit and different Reynolds numbers (a)  $1D_0$ , (b)  $2D_0$ , (c)  $3D_0$  at  $Re = 440$  ( $\square$ ),  $Re = 550$  ( $\circ$ ), and  $Re = 650$  ( $\triangleleft$ ). Here  $\omega_0 \sim U_0/(D_0/2)$  is a characteristic shear scale at the nozzle exit.

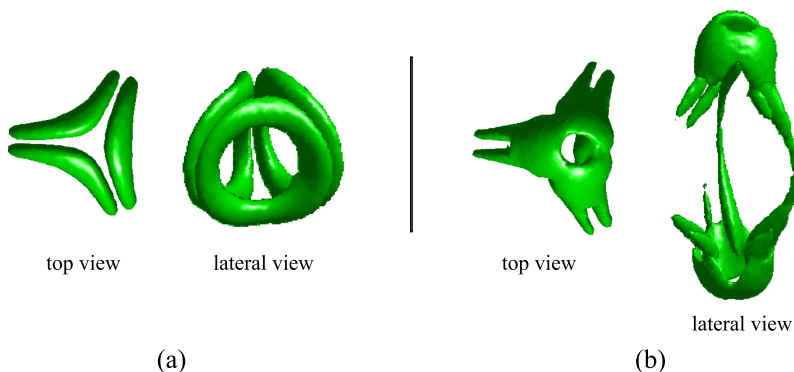


FIG. 7. 3R collision. Secondary structures produced by the collision of three rings. (a) The local pairing of vortex tubes dominates the first stages of the collision through the motion of dipolar arm-like structures which produce a rapid radial increase of the structure size ( $t = 0.65$  s) (secondary dipolar arms). (b) Finally, top and bottom vortex rings are formed ( $t = 1.45$  s) (secondary rings).

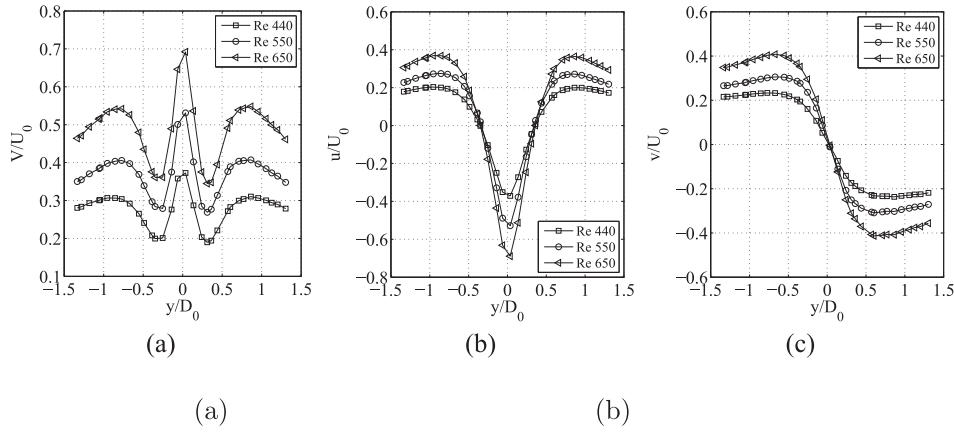


FIG. 8. 3R collision. Velocity profile through the transverse axis of a dipolar arm indicated in Fig. 7. (a) Velocity magnitude  $V = (v_x^2 + v_y^2)^{1/2}$ . (b) Velocity component  $v_x$  versus  $x$ -axis. (c) Velocity component  $v_y$  versus  $y$ -axis.

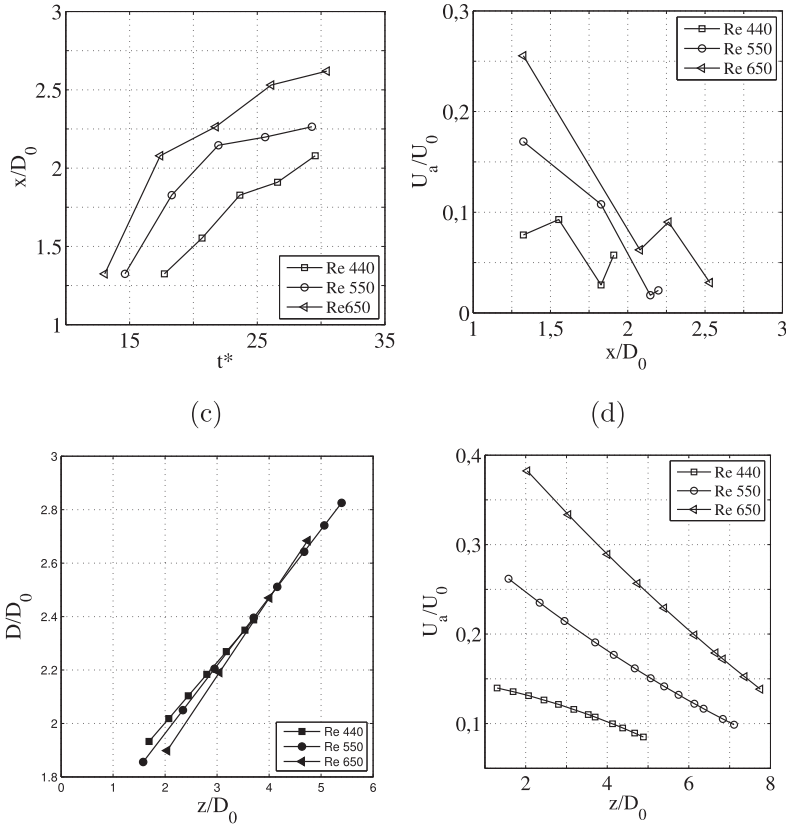


FIG. 9. 3R collision. (a) Time evolution of the position of one of the dipolar arms. (b) Spatial evolution of the dipolar arm velocity with distance  $x$ . (c) Spatial evolution the secondary ring diameter with  $z$ -axis. (d) Self-induced velocity of the secondary ring with  $z$ -axis.

Figures 9(a) and 9(b) show the evolution of the position and velocity of the secondary dipole, respectively. These structures are well influenced by  $Re$  as the greater the Reynolds number, the higher the expansion velocity of the structure. However, there is an evident damping of the motion as the structure grows in size as the slope increases with  $Re$  in Fig. 9(b).

Once those dipolar arms are formed, it follows the reconnection of the upper tubes of the rings, forming two new vortex rings that emerge on the  $z$ -axis, i.e., in a direction perpendicular direction with respect to the collision plane (defined by the paths of the primary rings). The initial shape of these rings is triangular (when viewed from above) due to the configuration of the collision and as the structure expands as a whole, the rings move away adopting a regular ring's shape. These new rings can also be characterised by their diameter and self-induced velocity as it is shown in Figs. 9(c) and 9(d), respectively.

It is clear that the secondary rings expand as they move away from the point of collision and that the greater the Reynolds number, the higher the speed they move in the  $z$ -axis.

In Fig. 10, we display the velocity contour map at different  $z/D_0$  locations (viewed from above). We observe the effect of the reconnection between top sections of the vortex tubes of the three rings, generating high velocity triangular-shaped vorticity structures traveling in the  $z$  direction in reasonable agreement with the experimental results of Ref. 5. The triangular shape observed at  $z/D_0 = 1$  and  $z/D_0 = 2$  finally evolves into a (bigger than original) vortex ring of diameter nearly  $2D_0$  when measured at  $z/D_0 = 3$ . This can be understood from the velocity profiles plotted on the axes  $\sigma_1$  and  $\sigma_2$  defined in each Fig. 10.

Note that if we join together the velocity profile from  $\sigma_1 \in (0, 4)$  and  $\sigma_2 \in (-4, 0)$  [on Fig. 10(b)], we are able to reconstruct the typical vortex ring profile like those of Fig. 5. It is clear that when these shape differences disappear, the ring evolves into a typical ring.

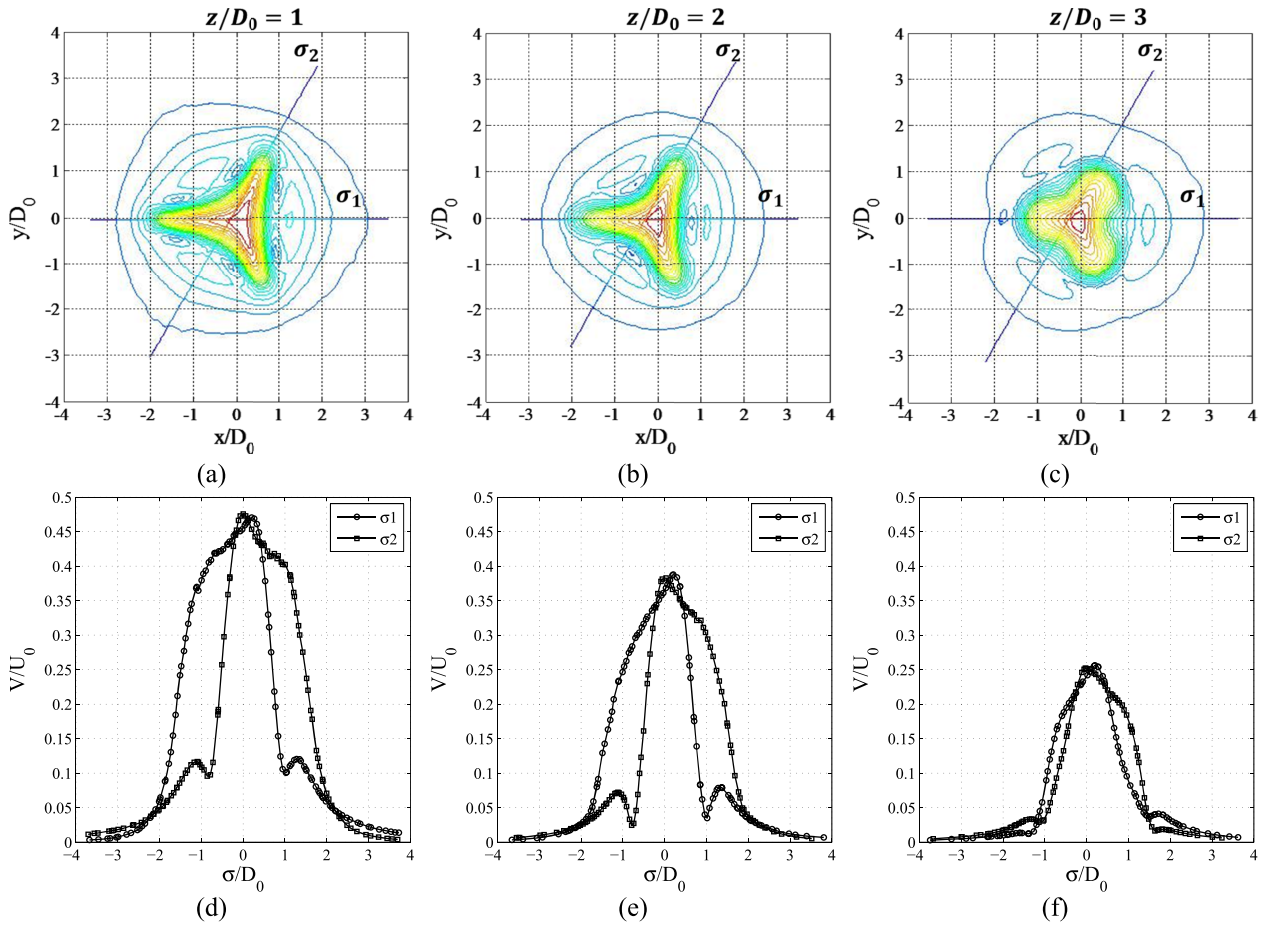


FIG. 10. Velocity contour maps (top) and normalised velocity profiles (bottom) of velocity magnitude,  $v = |\mathbf{v}(\mathbf{r})|$ , for the secondary vortex structures at [(a) and (d)]  $z = 1D_0$ , [(b) and (e)]  $z = 2D_0$ , and [(c) and (f)]  $z = 3D_0$  measured from the domain center.

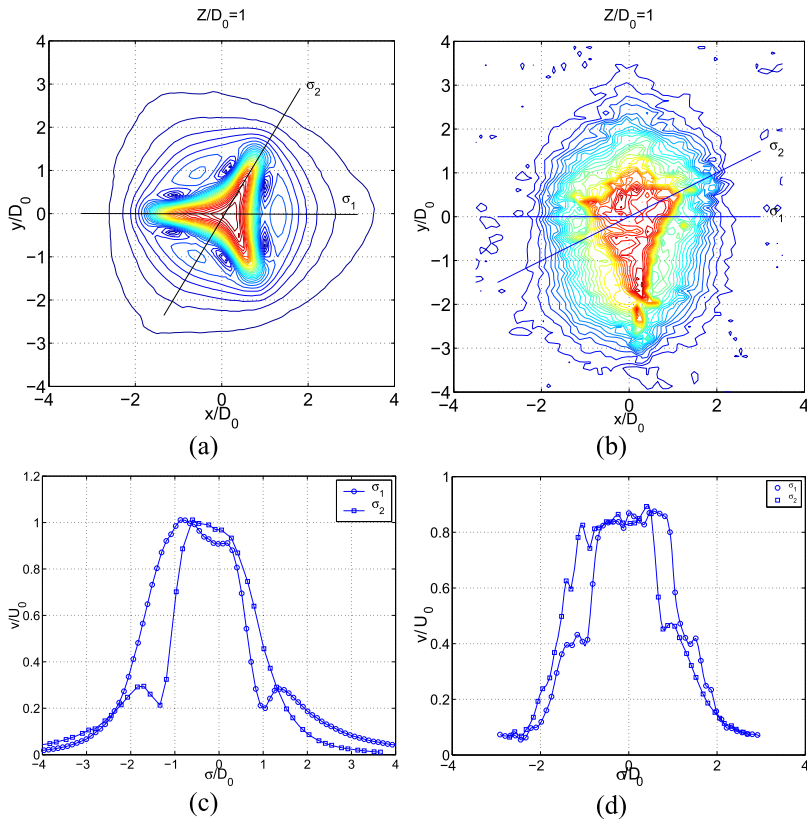


FIG. 11. Comparison between numerical (left,  $Re = 440$ ) and experimental results (right,  $Re = 320$ ) for 3 vortex rings in air after collision ( $t \sim 550$  ms). [(a) and (b)] Velocity contour map and [(c) and (d)] velocity magnitude profiles,  $v = |\mathbf{v}(\mathbf{r})|$ , for the secondary vortex structures at  $z = 1D_0$  measured from the domain center.

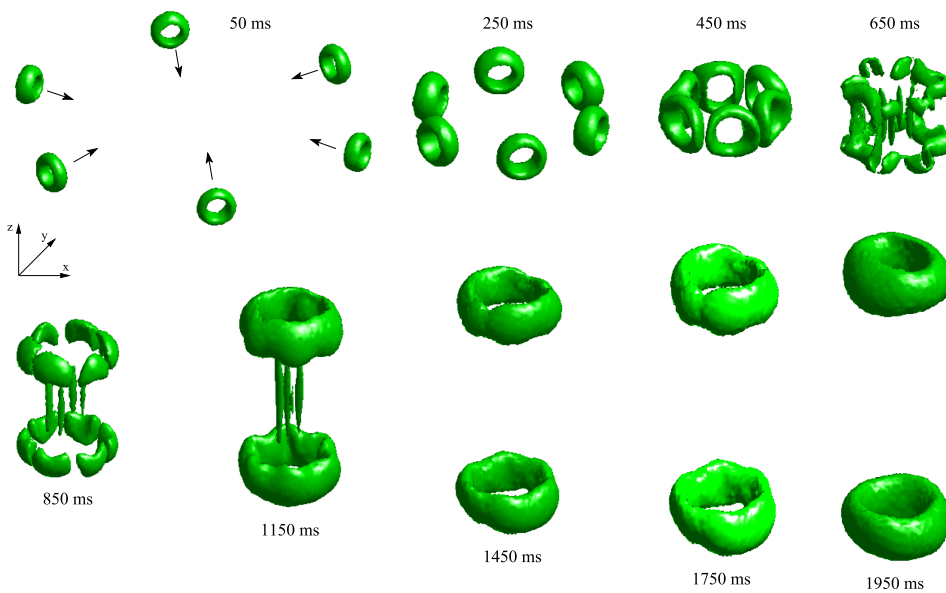


FIG. 12. 6R collision. Time evolution of the vorticity iso-surface  $|\omega(\mathbf{r}, t)| = 30\%$  of the maximum vorticity value found at each successive time after  $t_0$  in Eq. (4) for  $Re = 440$ . Multimedia view: <https://doi.org/10.1063/1.5004587.1>

We wanted to compare numerical and recent experimental results for the secondary vortex structures found.<sup>5</sup> In Fig. 11, we show the absolute velocity maps at  $z/D_0 = 1$  from the collision center. When we look at the details of the velocity profiles across the triangular-shaped vorticity structures, we notice the same effect already described in the paragraph above. We observe a fairly good agreement with the triangular shape of the secondary structure shown in Fig. 7 when looked from above. The velocity profiles shown correspond to the absolute value of the velocity  $v = |\mathbf{v}(\mathbf{r})|$ . It is important to consider all velocity components in order to take into account the rapid flow in the vertical direction. Otherwise the rough similarity observed is lost. The experimental velocity was measured with a hot wire anemometer.

## B. Collision of 6 rings (6R)

In this section, we study the collision between 6 identical rings launched simultaneously from each of the vortex generators. Figure 12 (Multimedia view) shows the temporal progression of the collision with the aid of the iso-surface plots of vorticity. As in the case of three rings, once the formation process is completed, the rings move in a straight path toward the collision zone ( $0.05 < t < 0.45$  s). An increase

in the characteristic diameter occurs as the rings approach to the collision zone, and similarly to the 3 rings case, the self-induced velocity  $U_a$  and the circulation are found to decrease progressively.

For  $0.65 < t < 1.15$  s, the vorticity lateral tubes of the rings make contact with a slight reconnection; however, the generation of dipolar arms is not observed. As in the collision of three rings, we also observe here the reconnection of the top and bottom vortex tubes of each ring. This gives life to two rings that emerge ejected in a direction perpendicular to the collision plane. This sequence of images reminds us an interesting experimental work<sup>1</sup> which reports the head-on collision of two rings that produce secondary structures in the form of multiple rings in radial motion perpendicular to that of the initial colliding rings. If we make use of a hypothetical time reversal of the collision, our case becomes reminiscent of Lim and Nickels' observations, but without a main ingredient which is in our collisions, we did not see the azimuthal instability.

### 1. 6R secondary structures

As it can be seen in Fig. 13, the reconnection of lateral vorticity tubes occurs with a smaller angle than in the case of

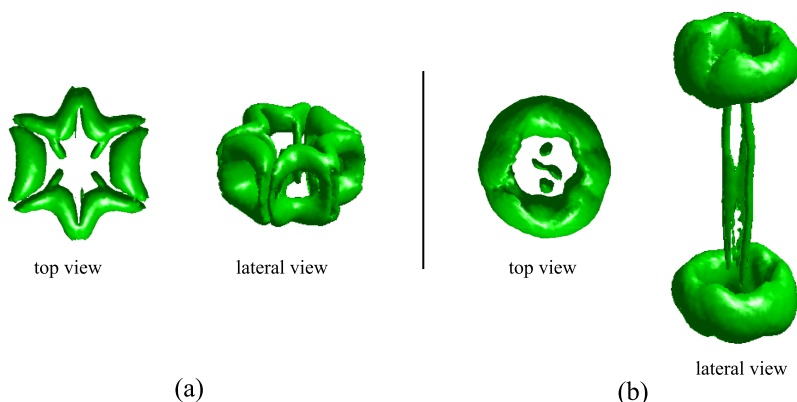


FIG. 13. 6R collision. Secondary structures produced by the collision of six rings at  $Re = 650$ . (a) A complex hexagonal secondary structure ( $t = 0.25$  s) evolves rapidly (secondary hexagonal arms) (b) into a top and bottom vortex rings ( $t = 0.65$  s). The irregularities of the rings may be the result of time dependent oscillations (secondary rings).

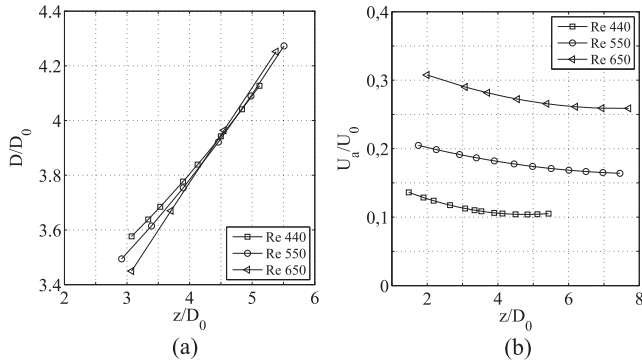


FIG. 14. 6R collision. (a) Ring diameter and (b) self-induced velocity as a function of the axial ring position.

three rings, which may explain why the generation of vorticity dipoles is not observed.<sup>7</sup> With respect to the reconnection of the upper vorticity tubes, the formation of two vorticity rings is now resulting from the star-like form having the same role of the triangular shape in the 3 rings case. The initial shape of the rings is determined by the configuration of the rings that collide, so the rings formed are hexagonal shaped at first and then, after some time, they evolve into two big rings moving perpendicular to the collision plane. Figures 14(a) and 14(b) show the evolution of the diameter and the velocity of the secondary rings resulting from the collision, respectively. The diameter of the rings increases linearly and can be as big ( $\sim 4D_0$ ) compared to the size of the secondary rings of the 3 ring collision case.

Secondary rings also display a reduction of the self-induced velocity as they move away from the collision zone. However  $U_a$  shows a flatter evolution than the 3 rings case, meaning that they keep moving for a long time.

### C. Pressure field

Within the many potential uses of the collision, for instance, as a 3D combustion chamber to control flame stretching<sup>24</sup> or as a vorticity control for combustible rings,<sup>25</sup> the pressure field must be analysed mostly in the central region of the collision. This zone, bounded by the incoming rings, will display a pressure field carrying the signature of the collision.

The pressure field is variable in time and space and depends heavily on the number of colliding rings, being very

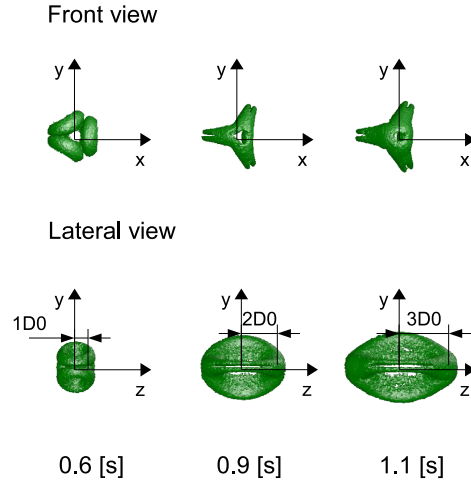


FIG. 15. 3R collision. Time evolution of vorticity iso-surfaces at  $|\omega| = 30\%$  of the maximum vorticity value at  $Re = 550$ . The time instants correspond to  $z \sim 1D_0, 2D_0,$  and  $3D_0$  from the collision center.

sensitive to the spatial symmetries of the process. For instance, depending on the case studied, we will observe zones of negative relative pressure which are important, for example, for particle trapping applications.

### 1. Pressure field in 3R

Figure 15 will help the reader to understand the pressure profile of this section and their evolution as a result of the collision. We will display the pressure profiles as a function of the three spatial coordinates. We will focus on the local pressure at the center zone of the collision for three characteristic time scales corresponding to  $1D_0, 2D_0,$  and  $3D_0$  from the collision center as indicated in Fig. 15 in order to track the effect of the secondary structures.

As the rings move toward the collision zone, local pressure at the collision center begins to increase rapidly, producing symmetries in the pressure profiles in  $y, z$  spatial coordinates in both 3R and 6R cases. In the 3R case shown in Fig. 16, we observe a symmetric pressure rise in the central zone which becomes nearly axisymmetric when the rings get closer to each other at nearly  $D_0$  from the collision center. After that, central pressure relaxes rapidly when the secondary structures start to move upward and downward leaving the collision zone.

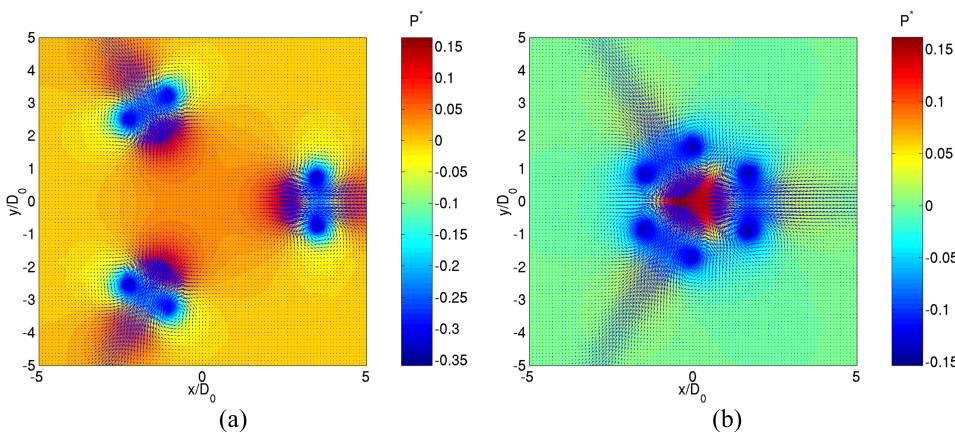


FIG. 16. 3R collision at  $Re = 440$ . Pressure distribution  $P^* = p(\mathbf{r}, t)/\rho U_a^2$  and vector velocity field at  $z/D_0 = 0$  for (a)  $t = 300$  (ms) and (b)  $t = 500$  (ms) where we observe an axisymmetric pressure bump around the collision center.

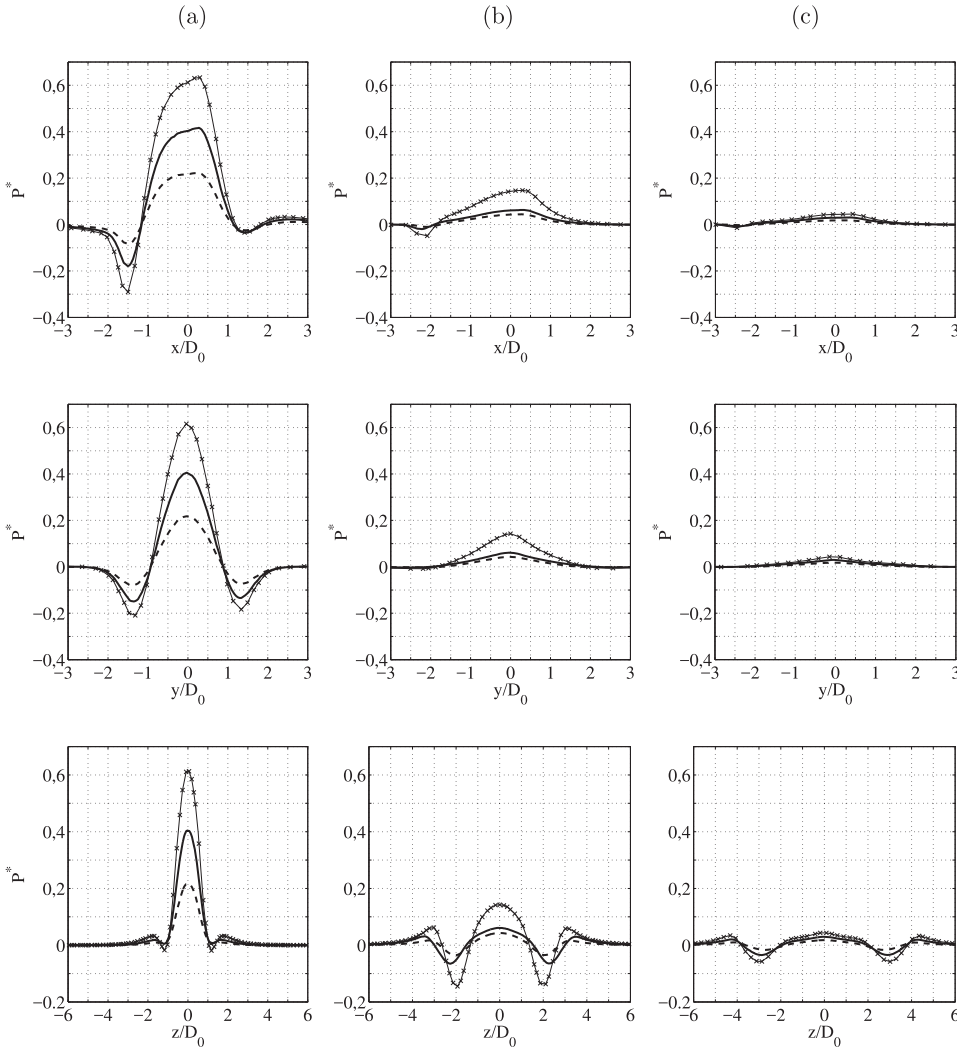


FIG. 17. 3R collision. Dimensionless relative pressure field profiles during the 3 ring collision at different distances from the collision center (a)  $1D_0$ , (b)  $2D_0$ , and (c)  $3D_0$  with  $P^* = p(\mathbf{r}, t)/\rho U_a^2$  and  $Re = 440$  (—),  $Re = 550$  (---), and  $Re = 650$  (-·-).

Figure 17 shows the total pressure across the  $x$ ,  $y$ , and  $z$  axes for the 3R collision at distances  $1D_0$ ,  $2D_0$ , and  $3D_0$  from the collision center. We first observe a pressure asymmetry across the  $x$ -axis as it can be inferred from Fig. 16. In the top row ( $x$ -axis), there is a maximum around the center of collision and two local minima, which indicate, in the negative half-axis, the presence of a dipolar arm which is formed where the pressure is negative. In the positive half-axis, we have the effect associated with high center velocity of the ring coming from the right nozzle.

In the middle row of Fig. 17, we show the evolution of the pressure across the  $y$ -axis. A maximum is observed in the collision center and two local minima indicating the position of the ring vortex tubes. Side-by-side rings begin to reconnect forming dipolar arms of vorticity. The magnitude of the pressure at the collision center through the  $y$ -axis decreases as those arm-like structures move radially away from the collision zone.

In the bottom row of Fig. 17, we found both positive and negative pressure zones related to the presence of the upper tubes of the rings that begin to reconnect forming the triangular shaped structures evolving into two rings which travel in the  $z$ -axis. In the center of collision, a maximum pressure is observed that decreases as the formed structures move away from the point of collision; however, it seems interesting to see that

the higher the  $Re$ , the deeper the negative wells found on the  $z$ -axis.

## 2. Pressure field in 6R collision

The symmetry of the pressure profiles in the 6R collision (Fig. 18) can be understood looking into Fig. 19 where we

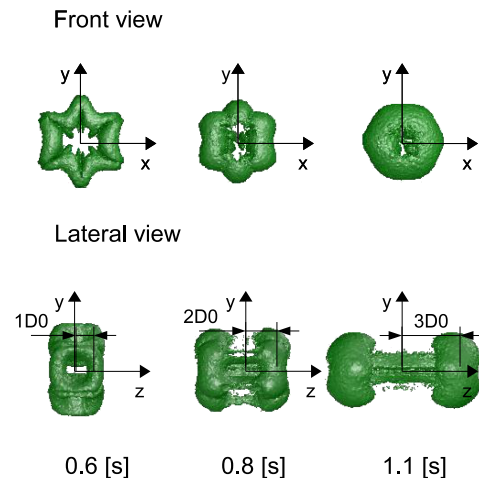


FIG. 18. 6R collision: Time evolution of vorticity iso-surfaces at  $|\omega| = 30\%$  of the maximum vorticity value at  $Re = 650$ . The time instants correspond to  $z \sim 1D_0, 2D_0$  and  $3D_0$  from the collision center.

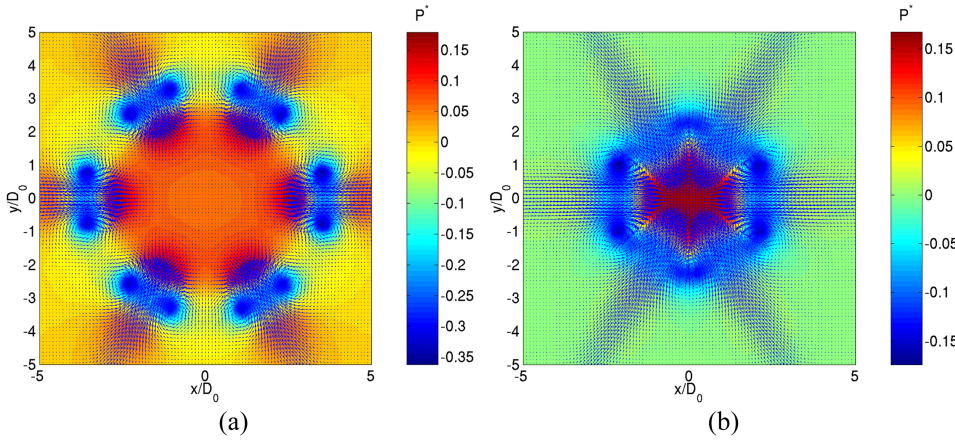


FIG. 19. 6R collision at  $Re = 440$ . Pressure distribution  $P^* = p(\mathbf{r}, t)/\rho U_a^2$  and vector velocity field at  $z/D_0 = 0$  for (a)  $t = 300$  (ms) and (b)  $t = 500$  (ms).

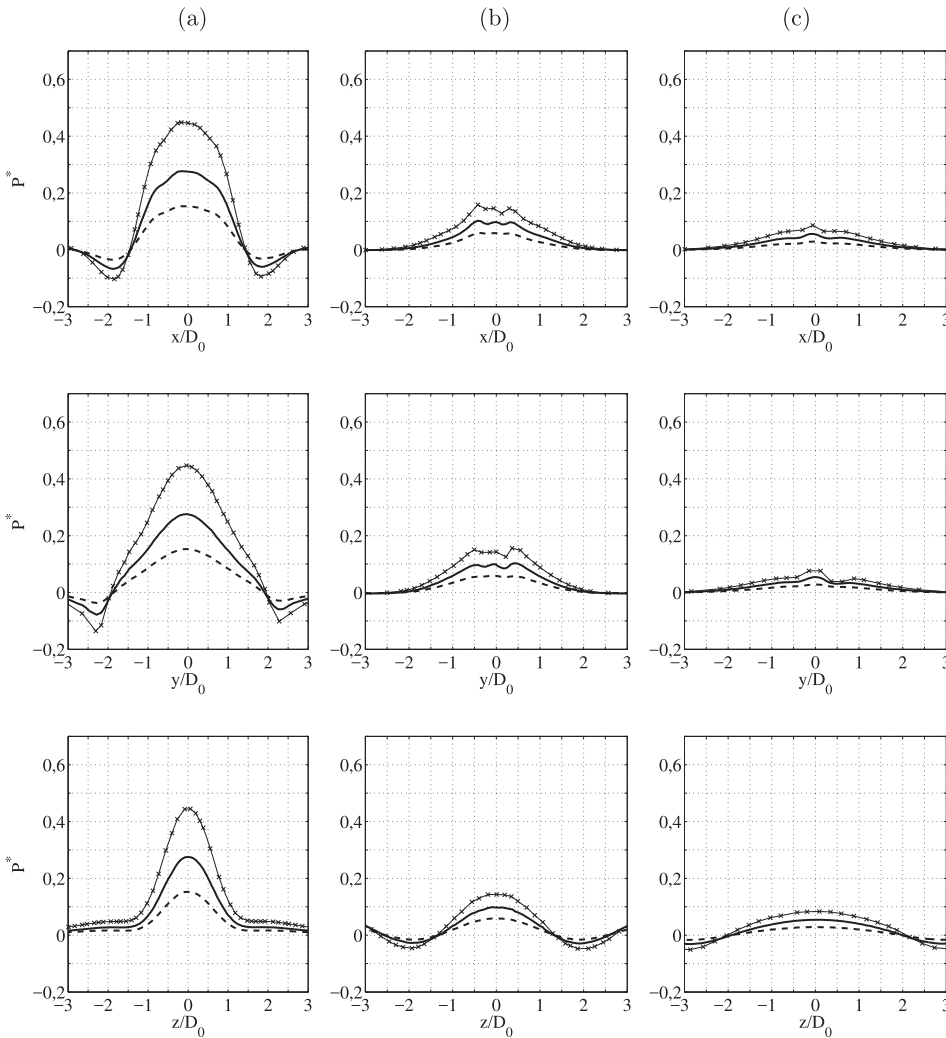


FIG. 20. 6R collision: Relative pressure profiles during the 6 ring collision at different distances from the collision center (a)  $1D_0$ , (b)  $2D_0$ , and (c)  $3D_0$  with  $P^* = p(\mathbf{r}, t)/\rho U_a^2$  and  $Re = 440$  (---),  $Re = 550$  (—), and  $Re = 650$  (-·-).

display the pressure and vector velocity field at mid height. The closer the neighboring rings, the higher the pressure rise. We observe a symmetric pressure rise in the central zone for higher distances from the collision center as the 6 rings come into contact before in the case of 3 rings. After that, when the secondary structures start to move upward and downward on the vertical coordinate  $z$ , pressure decreases rapidly.

Figure 20 (top row) shows the pressure across the  $x$ -axis, for collision of 6 vortex rings, at distances  $1D_0$ ,  $2D_0$ , and  $3D_0$  from the nozzle exit.

We observe symmetric profiles across the three spatial coordinates showing also typical central high pressure zone bounded by two local minima which represent the center of the rings coming from the nozzle that lies on the  $x$ -axis. If we compare with Fig. 17, we have lower amplitudes but the extension of the structure, defined by the size of the high pressure zone, appears clearly bigger than the corresponding 3R case. In this case, the local pressure begins to decrease rapidly when the secondary ring structures move away from the collision point.

We also note that negative pressure zones have weaker amplitudes than the 3R case. For instance, in Fig. 20 (middle row), a central maximum and two local minima are rapidly swept out at  $2D_0$  as a result of the reconnection of the hexagonal star-like secondary structure.

Both collision types display a central high pressure bounded by negative pressure zones that are swept out rapidly as the secondary structures dominate the mechanics of the collision. However, this kind of configuration allows us to create local and dynamic  $\pm p(\mathbf{r}, t)$  pressure zones in 3D space without the need of solid boundaries.

#### D. Kinetic energy of the collision

In this section, we analyse the kinetic energy of the collision in order to identify different stages, associating energy levels to each vortex structure, specially the secondary structures. The kinetic energy is calculated in the whole volume according to the expression

$$E_k(t) = \frac{1}{2} \rho \int |\mathbf{v}(\mathbf{r}, t)|^2 dV. \quad (9)$$

We considered three main time instants of the process representing the three most characteristic topological distributions of vorticity as shown in Fig. 21. (a) When the rings are completely formed and move in free flight into the collision center, (b) when the rings collide and vortex tube merging takes place, and (c) some instants after the collision when the secondary structures have already been formed.

To normalise the kinetic energy values, we simply used the kinetic energy of the fluid slug moving through the nozzle exit. If  $U_0$  is the nozzle exit velocity [cf. Eq. (7)],  $d\tau$  is the characteristic time duration of the piston stroke and  $L = U_0 d\tau$  is the slug length, then the fluid slug kinetic energy is

$$E_0 = \frac{1}{2} \rho U_0^2 (\pi D_0^2/4)L.$$

The kinetic energy  $E_k(t)$  calculated throughout the control volume for the configuration of three and six rings is summarised in Table II. A strong decay is observed in both collision and post-collision, and the magnitude of the energy of the 6R case is approximately double than that observed in the 3R case.

The results of Table II allow one to evaluate the evolution of kinetic energy only at a general level and it is not possible to detect energy fluctuations around the collision process at least in the first two stages. Even though, it is interesting to see a significant difference in the collision energy once the secondary structures start to evolve by their own dynamics.

To go into more details, we performed an alternative calculation of the kinetic energy per length using Eq. (10). The idea is to add the squared velocity values over a vorticity iso-surface  $\Omega = 0.3|\omega|_{\max}$  which is arbitrarily defined as the iso-vorticity curves at 30% of the maximum vorticity in every moment. This value allows us to plot a clear surface containing the ring's most characteristic structures,

$$E(t) = \int_{\Omega} |\mathbf{v}(\mathbf{r}, t)|^2 dS. \quad (10)$$

The energy curves obtained by this calculation are shown in Figs. 22 and 23 for three and six rings, respectively. It is possible to identify four zones on the energy curves of both figures within the collision process.

The first zone (I) corresponds to the ring formation process where the energy increases rapidly during the piston stroke reaching a global maximum which is determined by

TABLE II. Normalised kinetic energy at  $Re = 650$ , before, during, and after collision for both configurations corresponding to the time instants of Fig. 21.

$E_k/(nE_0)$	Before collision	During collision	After collision
$n = 3$ rings	3.75	1.35	0.47
$n = 6$ rings	3.70	1.51	0.95

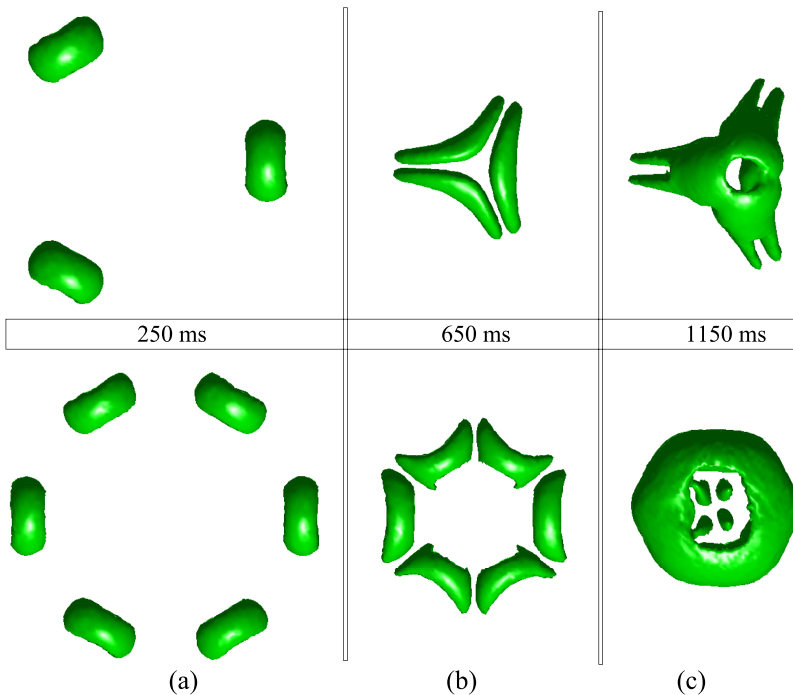


FIG. 21. 3R and 6R collisions. Top view of vorticity iso-surfaces at  $|\omega(\mathbf{r}, t)| = 0.3|\omega|_{\max}$  at  $Re = 440$  in order to compute the kinetic energy for 3 and 6 rings. (a) Before collision, (b) during collision, and (c) after collision.

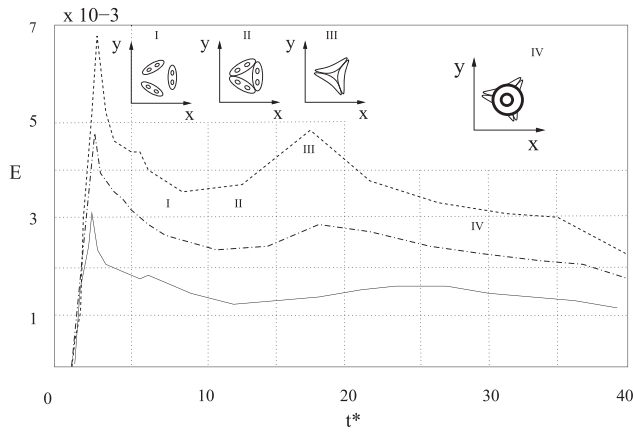


FIG. 22. 3R collision: Kinetic energy per unit length for vorticity iso-surface  $|\omega(\mathbf{r}, t)| = 0.3|\omega|_{\max}$ . We identify four zones: (I) The 3 incoming rings moving in free flight, (II) first contact between neighbour rings, (III) formation of secondary structures, and (IV) ejection of secondary rings in the direction perpendicular to the collision plane.  $Re = 440$  (continuous line),  $Re = 550$  (dot-dashed line), and  $Re = 650$  (dashed line).

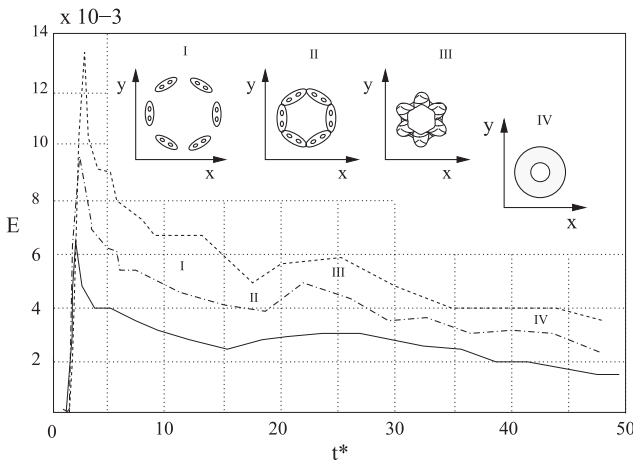


FIG. 23. 6R collision: Kinetic energy per unit length for vorticity iso-surface  $|\omega(\mathbf{r}, t)| = 0.3|\omega|_{\max}$ . We also identify four zones: (I) The 6 incoming rings moving in free flight, (II) first contact between neighbour rings, (III) formation of secondary ring structures, and (IV) ejection of secondary rings in the direction perpendicular to the collision plane.  $Re = 440$  (continuous line),  $Re = 550$  (dot-dashed line), and  $Re = 650$  (dashed line).

the value of the Reynolds number. Then a second zone (II) may be defined where an important energy drop occurs as the rings move towards the center of collision. After this zone, an energy increase is observed (III) when the rings begin to interact between them. In this zone, the local maximum is associated with the rapidly expanding arm-like dipolar structures of vorticity.

Finally we observe section (IV) where the mechanics of the collision is driven exclusively by the secondary structures.

#### IV. CONCLUSIONS

In this work, we have studied numerically in 3D two different symmetric collisions between laminar vortex rings. We have solved both mass and momentum conservation equations to investigate the motion, interaction, and simultaneous collision between many initially stable vortex rings. We

studied two main configurations: 3 and 6 rings making an angle of  $60^\circ$  and  $120^\circ$  between their straight path lines, respectively. Here we adopted a vortex generation method in order to mimic, as close as possible, the generation conditions for experimental vortex ring generators based on piston devices.

Our results are reported for laminar vortex rings in air solving the individual ring velocity, pressure, and vorticity fields, in free flight, during the entire collision and after the formation of new secondary structures. Each collision was studied for small Reynolds numbers  $Re < 10^3$  based on both the self-induced velocity and diameter of the ring. Our numerical results are in qualitative agreement with recent experiments in the case of 3 rings.<sup>5</sup> In general, the mechanics of the collision can be understood on the basis of the type of secondary structures resulting as a function of the local angle (bisecting) between neighbour colliding rings.<sup>7</sup> In the case of 3 rings, the collision forced a local pairing between adjacent vortex tubes of opposite circulation, which gives life to radially expanding secondary arm-like dipolar structures. These structures are accompanied with two secondary vortex rings moving in opposite directions, perpendicular to the collision plane.

In the case of 6 colliding rings, the bisecting angle between neighbour rings is smaller than the previous case and after collision we obtain only two vortex rings as secondary structures. These rings move in opposite directions, perpendicular to the collision plane, a process that reminds us the head-on collision of two vortex rings of Lim and Nickels<sup>1</sup> under a hypothetical time reversal transformation. Both kinds of collisions exhibit a systematic kinetic energy decay in the range of Reynolds numbers investigated here. The kinetic energy may display local increases as a result of the acceleration of the secondary structures observed in the case of 3 colliding rings.

#### ACKNOWLEDGMENTS

This work was supported by Fondecyt Grant No. 1085020. T. Reyes acknowledges CONICYT PFCHA/Beca Nacional de Magister Convocatoria 2013, 22131639.

- <sup>1</sup>T. T. Lim and T. B. Nickels, "Instability and reconnection in the head-on collision of two vortex rings," *Nature* **357**, 225–227 (1992).
- <sup>2</sup>P. Chatelain, D. Kivotides, and A. Leonard, "Reconnection of colliding vortex rings," *Phys. Rev. Lett.* **90**, 054501 (2003).
- <sup>3</sup>W. Hwang and J. K. Eaton, "Creating homogeneous and isotropic turbulence without a mean flow," *Exp. Fluids* **36**, 444–454 (2004).
- <sup>4</sup>S. Kida, M. Takaoka, and F. Hussain, "Collision of two vortex rings," *J. Fluid Mech.* **230**, 583–646 (1991).
- <sup>5</sup>R. H. Hernández and E. Monsalve, "Experimental observation of the collision of three vortex rings," *Fluid Dyn. Res.* **47**, 035513 (2015).
- <sup>6</sup>P. G. Saffman, "A model of vortex reconnection," *J. Fluid Mech.* **212**, 395–402 (1990).
- <sup>7</sup>T. Fohl and J. S. Turner, "Colliding vortex rings," *Phys. Fluids* **18**, 433–436 (1975).
- <sup>8</sup>Y. Oshima, "Head-on collision of two vortex rings," *J. Phys. Soc. Jpn.* **44**, 328–331 (1977).
- <sup>9</sup>M. Gharib, E. Rambod, and E. Shariff, "A universal time scale for vortex ring formation," *J. Fluid Mech.* **360**, 121–140 (1998).
- <sup>10</sup>J. P. Sullivan, S. E. Widnall, and S. Ezekiel, "Study of vortex rings using a laser doppler velocimeter," *AIAA J.* **11**, 1384–1389 (1973).
- <sup>11</sup>R. H. Hernández, B. Cibert, and C. Béchet, "Experiments with vortex rings in air," *Europhys. Lett.* **75**, 743–749 (2006).

- <sup>12</sup>G. Arévalo, R. H. Hernández, C. Nicot, and F. Plaza, "Vortex ring head-on collision with a heated vertical plate," *Phys. Fluids* **19**, 083603 (2007).
- <sup>13</sup>A. Michalke, "Survey on jet instability theory," *Prog. Aerosp. Sci.* **21**, 159–199 (1984).
- <sup>14</sup>S. James and C. K. Madnia, "Direct numerical simulation of a laminar vortex ring," *Phys. Fluids* **8**, 2400–2414 (1996).
- <sup>15</sup>I. Danaila and J. Hélie, "Numerical simulation of the postformation evolution of a laminar vortex ring," *Phys. Fluids* **20**, 073602 (2008).
- <sup>16</sup>R. H. Hernández and G. Rodríguez, "Passive scalar transport mediated by laminar vortex rings," *Fluid Dyn. Res.* **49**, 025514 (2017).
- <sup>17</sup>R. Sau and K. Mahesh, "Passive scalar mixing in vortex rings," *J. Fluid Mech.* **582**, 449–461 (2007).
- <sup>18</sup>Fluent, ANSYS FLUENT 12 Theory Guide, 2009.
- <sup>19</sup>S. V. Patankar, *Numerical Heat Transfer and Fluid Flow* (Hemisphere Publishing Corporation, Washington, D.C., 1980).
- <sup>20</sup>I. B. Celik, G. Urmila, P. J. Roache, C. J. Freitas, H. Coleman, and P. E. Raad, "Procedure for estimation and reporting of uncertainty due to discretization in CFD applications," *J. Fluids Eng.* **130**, 078001 (2008).
- <sup>21</sup>P. G. Saffman, "The velocity of viscous vortex rings," *Stud. Appl. Math.* **49**, 371–380 (1970).
- <sup>22</sup>I. S. Sullivan, J. J. Niemela, R. E. Hershberger, D. Bolster, and R. J. Donnelly, "Dynamics of thin vortex rings," *J. Fluid Mech.* **609**, 319–347 (2008).
- <sup>23</sup>R. J. Donnelly, "Dynamics of vortex rings in viscous fluids," *Theor. Comput. Fluid Dyn.* **24**, 433–435 (2010).
- <sup>24</sup>C. J. Mueller, J. F. Driscoll, D. L. Reuss, M. C. Drake, and M. E. Rosalik, "Vorticity generation and attenuation as vortices convect through a premixed flame," *Combust. Flame* **112**, 342–358 (1998).
- <sup>25</sup>S. Ishizuka, T. Murakami, T. Hamasaki, K. Koumura, and R. Hasegawa, "Flame speeds in combustible vortex rings," *Combust. Flame* **113**, 542–553 (1998).